IEEE Access
Multidisciplinary | Rapid Review | Open Access Journal

Received August 29, 2019, accepted September 11, 2019, date of publication September 16, 2019, date of current version October 3, 2019.

Digital Object Identifier 10.1109/ACCESS.2019.2941511

Segmentation of Lung in Chest Radiographs Using Hull and Closed Polygonal Line Method

TAO PENG[1], YIHUAI WANG[1], THOMAS CANHAO XU[1], (Member, IEEE), AND XINJIAN CHEN[2,3], (Senior Member, IEEE)

[1]School of Computer Science and Technology, Soochow University, Suzhou 215006, China
[2]School of Electrical and Information Engineering, Soochow University, Suzhou 215006, China
[3]State Key Laboratory of Radiation Medicine and Protection, Soochow University, Suzhou 215123, China

Corresponding authors: Tao Peng (sdpengtao401@gmail.com), Yihuai Wang (yihuaiw@suda.edu.cn), Thomas Canhao Xu (thomasxu@suda.edu.cn), and Xinjian Chen (xjchen@suda.edu.cn)

This work was supported in part by the 2nd Hospital of Soochow University, in part by the National Science Foundation of China under Grant 61672369 and Grant No.61872257, in part by the National Natural Science Foundation of Jiangsu Province under Grant 17KJB520035 and Grant 17KJB520037, and in part by the Priority Academic Program Development of Jiangsu Higher Education Institutions (PAPD).

ABSTRACT Accurate lung segmentation in chest radiographs is a challenging problem due to the presence of strong edges at the rib cage and clavicle, the varying appearance in the upper clavicle bone region, too small costophrenic angle and the lack of a consistent anatomical shape among different individuals. In this paper, we propose a hybrid semi-automatic method called Hull-Closed Polygonal Line Method (Hull-CPLM) to detect the boundaries of the lung Region of Interest (ROI). To the best of our knowledge, this is the first attempt at lung segmentation using the Hull-CPLM in chest radiographs. The proposed method has two main steps: 1) an image preprocessing method is constructed to implement the coarse segmentation by using as low as 15% of the manually delineated points as the initial points, 2) a refinement step is used to fine-tune the segmentation results based on the improved principal curve model and the machine learning model at the refinement step. To prove the performance of the proposed method, both the private and public databases were used. The private database is used to select the optimal parameters for the proposed method, where the result showed a good performance with the Dice Similarity Coefficient (DSC) as high as 97.08%. While on the public databases, our proposed algorithm not only surpassed the performance of different hybrid algorithms but also reached superior segmentation results by comparing with state-of-the-art methods.

INDEX TERMS Lung segmentation, chest radiographs, principal curve, closed polygonal line method, database, machine learning.

I. INTRODUCTION

Pulmonary cancer is one of the leading causes of death and hospitalization worldwide [1]. The lung images are always used for monitoring and analyzing the organ, which is an important strategy for the early diagnosis of pulmonary cancer [2], [3]. In the early stage of lung cancer, the radiologists can be assisted with the Computer Aided Diagnosis system (CAD) to detect abnormal tissue areas of the lungs, so as to improve diagnostic accuracy. Accurate lung segmentation is often performed as a necessary stage on quantitative and qualitative lung image analysis because it is important for identifying lung cancer in clinical evaluation. Hence, research on lung segmentation has always received much attention. Researches have proposed several algorithms for lung segmentation in recent years [4]–[6], while accurate lung segmentation continues to require more attention because of the heterogeneity of the organ.

Because of the low radiation and cost, chest radiographs are widely used for the diagnosis of pulmonary diseases. However, there are various anatomical challenges in Chest X-Ray (CXR) segmentation because of the following reasons, which are depicted in FIGURE 1: (1) For lung segmentation, it is a challenge that the edges at the rib cage and clavicle region result in local minima for many optimization methods. (2) There is another difficult issue for segmenting the lung apex because of the varying appearance in the upper clavicle bone region. (3) Other challenges include segmenting the

The associate editor coordinating the review of this manuscript and approving it for publication was Jeonghwan Gwak.

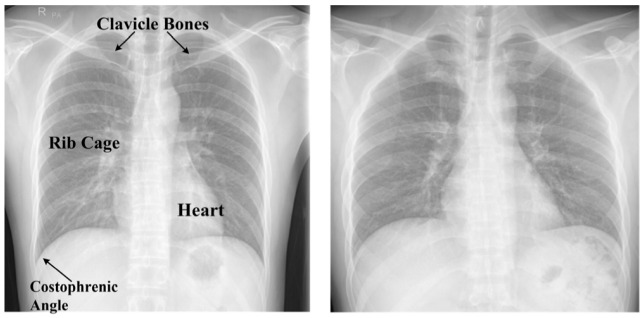

FIGURE 1. Anatomical feature in two chest X-ray images and their variations. Different lung shape, strong edges of the rib cage, visible heart shape, intensity variation around the clavicle bones, and sharp corner at the costophrenic angle that make the accurate lung segmentation to be a challenge. Both chest X-ray images are from the hospital database (see Section III-A).

small costophrenic angle, considering for anatomical shape inconsistencies among different individuals such as changeable heart dimensions or other pathology, and X-ray imaging inhomogeneities.

In the field of medical image processing, several algorithms are categorized as feature classify approaches [7]–[9], region segmentation approaches [10], [11], and contour extraction approaches [12], [13]. In [14], Shen *et al*. have developed a two-way chain coding model combined with a Support Vector Machine classifier (SVM) to minimize the over-segmentation of neighboring regions. The average over-segmentation rate of this model is as low as 0.3%, while it sometimes fails to re-include the juxtapleural nodules sitting in consolidation regions. Ahmad *et al.* [15] have developed a Content-Based Medical Image Retrieval System (CBMIRS) for lung segmentation and validated on the public JSRT dataset. However, the mean Jaccard similarity coefficient is only 0.870. Pratondo *et al*. [16] have integrated several machine learning models with region-based active contour models to segment medical images. Compared with the previous two approaches, the experimental results obtained by the contour extraction model can show the more realistic shape of the specific object, while it can reduce time complexity and save more storage space.

The critical goal of the contour extraction approach is to utilize a shape representation or curve approximation model to approximate the contour of the specific object. Using the Hedgehog shape prior, Isack *et al*. [17] have proposed the Potts model to complete the multi-object segmentation such as the lung, and obtain the segmentation result with high accuracy, while the model is not compared with state-of-the-art models. A unified segmentation model is proposed based on the Fully Convolutional Neural Network (FCNN) and the Shape Representation Model (SRM) [18]. However, the training and testing datasets are limited. In [19], Shi *et al*. have proposed a multilevel local region-based Sparse Shape Composition method (SSC) for liver segmentation. However, some region information is ignored since it begins with a blood vessel-based liver shape to be prior initialization.

Recently, the principal curve approach has gained a growing interest in segmenting abnormal organs from other neighboring normal structures, due to its strong abilities to effectively deal with noise input and obtain robust results [20]. The principal curve is defined as the ''middle'' of the one-dimensional curve passing through the set of the n-dimensional data points, providing a smooth and linear description of the *n*-dimensional dataset [21]. Through the description of the principal curve, it is known that the method is a more reasonable choice in the contour extraction algorithm. Khedher *et al*. [22] have used the principal curve algorithm and support vector machine for MRI images segmentation, while Li *et al*. [23] have devised the principal curve model to extract coronary artery and detect vessel, both of them have high accuracy to detect tissue contours. Further, the machine learning model as a classifier can be utilized for early diagnosis [24], [25]. Therefore, combining machine learning with the principal curve model can become a promising research hotspot in the field of disease detection [26].

In this work, we use less than 15% points of ROI as the approximate initialization, where 15% is an estimated value. A hybrid semi-automatic Hull-Closed Polygonal Line Method (Hull-CPLM) is proposed to obtain the smooth contour of the lung Region of Interest (ROI), which combines the preprocessing step and the refinement step. The preprocessing step of the proposed method utilizes the Hull consisting of Convex Hull Method (CHM) and ConCave Hull Method (CCHM) to implement the coarse lung segmentation. However, the Hull method is insufficient in correctly segmenting because of the variety of the scall parameter, so that the second step of the proposed method called the refinement step is employed necessarily. The innovation of the refinement step relies on combining the improved CPLM with the Backpropagation Neural Network Method (BNNM). The CPLM is used to obtain the data sequences to express a new curve which consists of line segments. The BNNM is used to provide the parameters for the smooth and unified mathematical expression of the lung ROI contour, while it is used for training to minimize the global error and achieve segmentation results with high accuracy.

The key contribution of our method can be summarized as follows. (1) It is the first attempt where several hybrid methods are combined for accurate lung segmentation in chest radiographs by using a few points as the approximate initialization. (2) Compared with the traditional Polygonal Line Method (PLM), the improved CPLM is first proposed by using a different initial way and adding several constraints and conditions. (3) The smooth and unified mathematical expression of the lung ROI contour is firstly presented. (4) To the best of our knowledge, this is the first attempt that the principal curve has been used for lung contour extraction, and the results are validated using up to five datasets (one private dataset, four public datasets).

The rest of the paper is organized as follows. We describe the proposed method in Section II. After that, Section III shows the quantitative and qualitative comparisons and

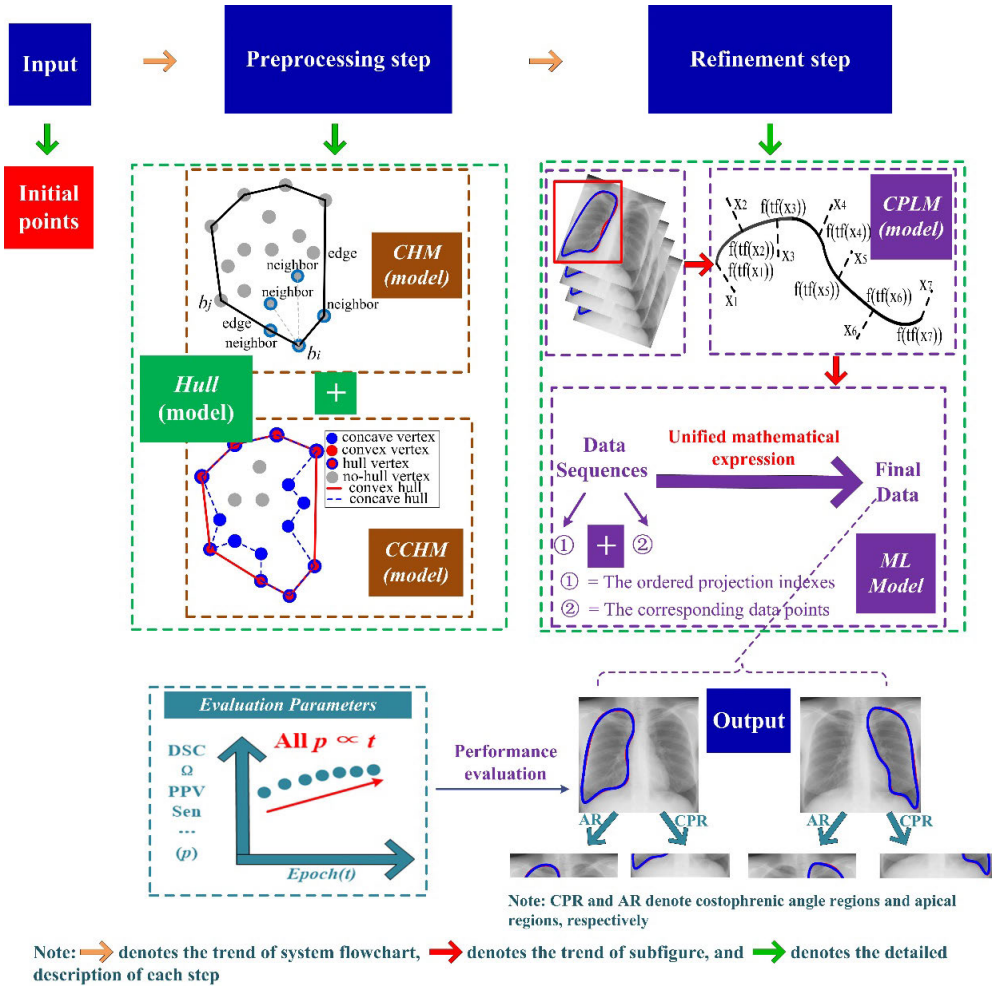

FIGURE 2. The flowchart of the proposed method. The system is divided into two parts, which are the workflow part and performance evaluation part, respectively. The workflow part consists of the preprocessing step and the refinement step. The preprocessing step consists of the CHM and CCHM, it can be used to find the extreme points and obtain the outer contour approximately. The refinement step combines the improved CPLM and the ML model, which is used to attain the smooth contour. The output can be quantitatively and qualitatively analyzed by the performance evaluation part.

evaluates the performance using both private hospital and public databases. Finally, a brief conclusion in Section IV is presented.

II. METHODS

Appropriate lung segmentation is expected to maximize the analytical possibilities and accurately identify normal and diseased tissues. In this paper, the proposed Hull-CPLM is a hybrid method consisting of several methods, which are applied sequentially. Images collected from mobile and X-ray scanners produce a different kind of CXR images. Therefore, a robust method that consists of the preprocessing step and refinement step is used to overcome this issue. The flowchart of the proposed algorithm can be shown in FIGURE 2.

A. PREPROCESSING STEP

When we deal with the disordered initial points, we use a new model called the Hull as the preprocessing step to achieve the approximate contour of the dataset, where the Hull consists of the CHM and CCHM. The CHM can find the extreme points to obtain the outer contour approximately, and the CCHM is always used to capture the exact shape of the surface of a dataset.

1) CONVEX HULL MODEL (CHM)

The initial points are defined as $S = \{x_1, x_2 \cdots x_n\}$, $x_i \in R^d$ and the initial segmentation results achieved by the preprocessing step of the proposed Hull-CPLM is defined as $B = \{b_1, b_2 \cdots b_n\}$, $b_i \in R^d$, the following equation can be written as:

$$B(b) = CH(b) \cup CCH(b) \tag{1}$$

where CH(b) is the vertex set of the convex hull, and CCH(b) is the vertex set of the non-convex (concave) hull.

In order to obtain the final outer contour, the CHM is mainly used to find all the extreme points along the boundary

Algorithm 1 Convex Hull (CHM)

Input: the initial dataset W
Output: the point list of the convex hull
Let b_0 be the point in W with the minimum y-coordinate(choose the minimum x-coordinate point when the y-coordinate of several points is the same)
Let $(b_1, b_2, \cdots, b_m)$ be the remaining points in W, sorted by the polar angle in counterclockwise order around b_0 (if more than one point has the same angle, remove all but the one that is farthest from b_0)
if m < 2
  return
else
  for $i = 2$ to m
    if (the orientation of three points is counterclockwise, which is b_{j-1} next to top in S, b_j at the top of S, and b_i, respectively)(see Eq.(2))
      pop point b_i stack
    push point b_i to stack
  end

of the convex hull. The principle of finding the extreme points is that calculates the direction of the intersection of the two vectors by Graham scan [27].

The details of the CHM are given in Algorithm 1. The specific search process is shown in FIGURE 3. The counterclockwise of three points can be determined as the following,

$$\overrightarrow{b_{j-1}b_j} \times \overrightarrow{b_{j-1}b_i} = (x_j - x_{j-1})(y_i - y_{j-1}) - (y_j - y_{j-1})(x_i - x_{j-1}) < 0 \quad (2)$$

where $b_{j-1}(\mathrm{x_j}_{-1}, \mathrm{y_j}_{-1})$ denotes the point at the top of S, $b_j(\mathrm{x_j}, \mathrm{y_j})$ denotes the point next to top of S, and $b_i(\mathrm{x_i}, \mathrm{y_i})$ is the point ready to stack. $\overrightarrow{b_{j-1}b_j} \times \overrightarrow{b_{j-1}b_i}$ is the cross product of the two vectors $\overrightarrow{b_{j-1}b_j}$ and $\overrightarrow{b_{j-1}b_i}$.

2) CONCAVE HULL MODEL (CCHM)

Combining with the obtained convex hull vertexes, we will use the CCHM to delineate the concave hull. The degree of delineating the concave hull depends on the size of the threshold n. The non-discrete dataset is determined repeatedly, and the convex hull is transformed into the concave hull. It is worth noting that if the threshold n is too small, the obtained contour can be too sharp. If the threshold n is too large, our algorithm does not perform "dig" operation, then the convex hull is still performed instead of the concave hull. Therefore, the selection of the optimal threshold n determines the smoothness of the lung contour surface.

The proposed CCHM consists of four steps. Firstly, a convex hull edge $(\mathrm{c_1}, \mathrm{c_2})$ can be selected and the threshold n is determined. Then, the point P closest to the $(\mathrm{c_1}, \mathrm{c_2})$ is chosen, where the P is located inside the convex hull. The distance $\mathrm{d_1}$ and $\mathrm{d_2}$ can be calculated, which are from the P to the vertex $\mathrm{c_1}$ of the $(\mathrm{c_1}, \mathrm{c_2})$ and the vertex $\mathrm{c_2}$ of the $(\mathrm{c_1}, \mathrm{c_2})$, respectively. And the shorter one of both distances is regarded as the decision distance d. Then comparing with threshold n, we can judge whether to "dig" or not. Finally, the iteration is

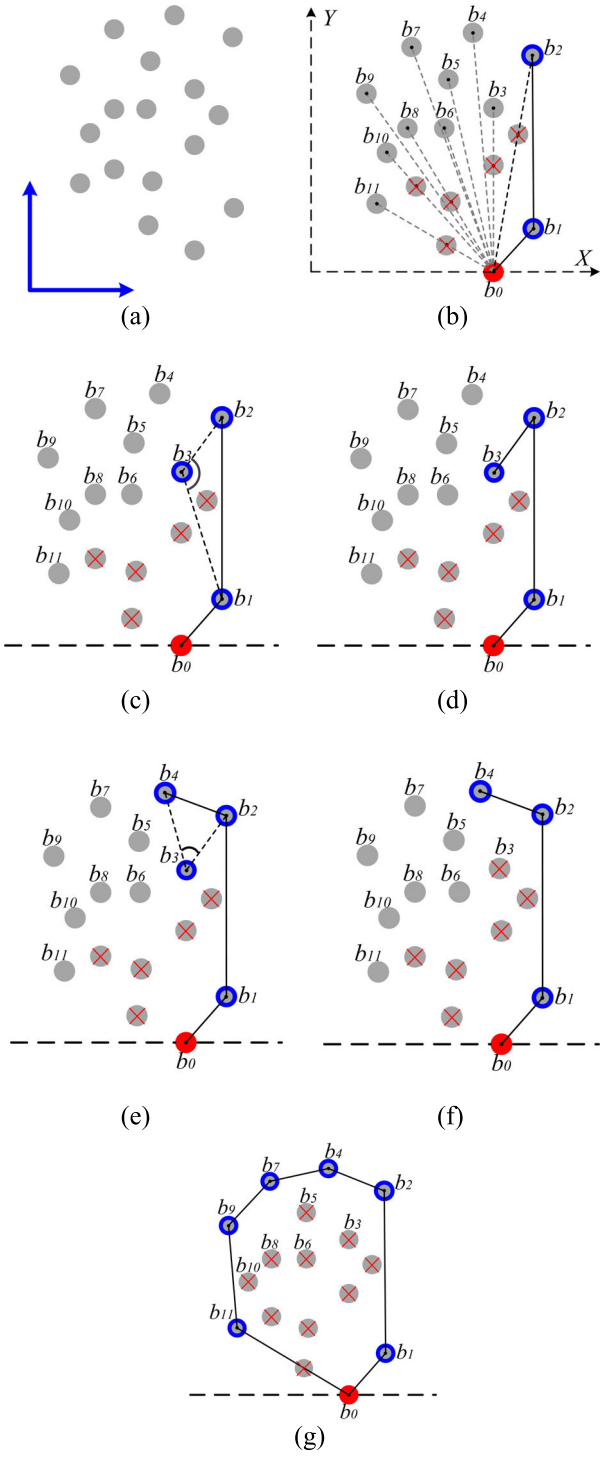

FIGURE 3. The process of obtaining the convex hull. The initial points are shown in (a). In (b), we remove some points that do not satisfy the condition (see Algorithm 1) and mark the red "X", then connect the points in the stack. In (c) to (e), we firstly select a new point from the remaining points and push it into the stack, and then we judge whether the new point will be retained according to the principal of the direction of the points (see Algorithm 1), finally the new point is remained in (f). The convex hull can be obtained shown in (g).

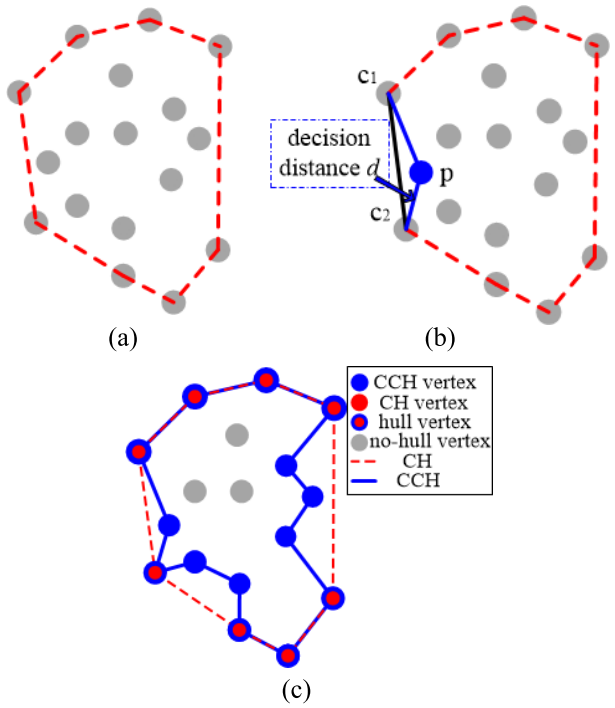

FIGURE 4. A flow diagram of obtaining the concave hull.

repeated until all the inside points are searched. The specific process of automatically obtaining concave hull contour is shown in FIGURE 4. The details of the Hull (Hull or CHM-CCHM) are given in Algorithm 2.

From the above discussion, the smoothness of the concave hull is influenced by the threshold n. With several experiments, we found that the valid range of n is in [0, 4], and the model has the best performance when n is 2. In most cases, if $N > 4$, the process of delineating the concave hull will not work and the concave hull is the same as convex hull.

B. REFINEMENT STEP

Considering the uncertainty of the results of the Hull, such as the degree of concave hull changes with the threshold size [28], we choose the principal curve model to solve the issue. The principal curve can reflect the real contour of the dataset, which is defined by Hastie and Stuetzle [29] as a smooth curve that passes through the middle of the data. In order to obtain the higher precision contour, the preprocessing segmentation results will be fine-tuned by the refinement step that combines the CPLM with the BNNM. The CPLM is used to find the data sequences that consist of the ordered projection indexes and the corresponding data points, then a new closed curve which consists of line segments can be expressed. Finally, a smooth mathematical model of the lung ROI contour is shown by the parameters of the BNNM, while the BNNM can be used for training to minimize the global error to obtain high precision results.

Algorithm 2 Convex-Concave Hull (Hull or CHM-CCHM)

Input: the initial dataset W
Output: the segmentation results T achieved by the preprocessing step (the Hull)
Preprocessing:
generate the coordinate of convex list V **// using the CHM**
choose the threshold n
copy convex list V to concave list C
Generating concave hull:
for $i = 1$ to the whole concave list C
  find the nearest inner point $p_k \in C$ from the edge (c_{i1},c_{i2}) where p_k should not be closer to neighbor edges of (c_{i1},c_{i2}) than (c_{i1},c_{i2})
  obtain the length of the edge $x = d(c_{i1},c_{i2})$
  obtain the decision distance $y = (p_k,\{c_{i1},c_{i2}\})$
    if $(x/y) > n$ **// Generating concave hull process where n is the threshold**
    insert new edges (c_{i1}, p_k) and (c_{i2}, p_k) into the tail of the concave list C
  delete edge (c_{i1},c_{i2}) from the concave list C
return the segmentation results T achieved by the Hull

1) CLOSED PRINCIPAL CURVE MODEL

Since the traditional Polygonal Line Model (PLM) proposed by Kegl *et al.* [30] cannot correctly describe the projection index of the dataset, the improved Closed Polygonal Line Model (CPLM) is proposed to obtain K-segment principal curve [30], which uses a closed square as the initial curve and add some constraints and stopping conditions to ensure the optimization of the model. We use the CPLM by inserting new vertexes to adjust the curve, which satisfied the principle of minimizing the penalty distance function [31]. The flowchart of the CPLM is shown in Algorithm 3.

The preprocessing segmentation result is defined as $T = \{t_1, t_2 \cdots t_n\}$, $t_i \in R^d$, where t_i is one point of the T. Firstly, we initialize the first principal component line, where it begins with a closed square which consists of line segments. From the counter-clockwise direction, the coordinates of the vertexes of the initial square are $\{(0.1, 0.1), (-0.1, 0.1), (-0.1, -0.1), (0.1, -0.1), (0.1, 0.1)\}$. Then we normalize the initial dataset T into the range of $\{(-1,-1) \sim (1,1)\}$ for unifying the dataset. After processing by the CPLM, the data sequences and a new closed curve can be finally achieved, where each point of the T is projected to the new closed curve. The data sequences are shown as $D = \{d_1,d_2 \cdots d_n\} \in R^d = \{(p_i, (x_i, y_i)), i = 1, 2 \cdots, n, 0 \leqslant p_1 < p_2 < \cdots < p_n \leqslant 1\}$. Where the projection index is $p_i \in P$, and the coordinate of the point is $(x_i, y_i) \in N$.

With the added constraint conditions, the optimal position of each vertex, the most favorable selection of the added line segment and the optimal shape of the obtained contour curve can be determined. When inserting a new vertex, the whole dataset is projected to the segment line and the determined vertexes, then the distance function from data points to the

curve can be calculated. The position of each vertex will be adjusted only if the value of the distance function becomes smaller. At the same time, the longest segment line containing the most projection points will be chosen. The shape of the contour curve is always closed during the process, and the angle between the lines on the curve is $90° < \theta < 180°$.

From the view of the stop conditions, the value of the current distance function is compared with that of the last inner loop distance function, and when the reduced value is less than the maximum distance deviation $\Delta s = 0.002$, the inner loop will exit. Comparing the value of the current distance function with that of the last outer loop distance function, when the reduced value is less than the maximum distance deviation $\Delta s = 0.002$, the outer loop will exit. The distance deviation Δs is determined by carrying out practical experiments. The number of line segments k is determined by the size of the input dataset, which cannot be increased indefinitely. The whole loop will terminate when $k > c\left(n, \Delta_n(f_{k,n}) = \beta * n^{1/3} r * (\Delta_n(f_{k,n})^{-1/2})\right)$ and the optimal solution of β reaches 0.3 [30].

2) SMOOTH MATHEMATICAL MODEL OF LUNG ROI CONTOUR

The data sequence obtained by the CPLM is expressed as $D = \{(p_i, c_i), i = 1, 2 \cdots, n, p_1 < p_2 < \cdots < p_n\}$, where the projection index is $p \in P$, and the coordinate of the point is $c(x,y) \in T$. In this way, (p, c(x,y)) can be understood as a causal relationship. We can regard x and y as the continuous function $x(p)$ and $y(p)$ on p, respectively, where the projection index p is regarded as the independent variable, and the coordinate of the point c(x,y) is the dependent variable.

A smooth and unified mathematical model can be found to express the relation of the parameters of the machine learning model while combining the machine learning model for training to minimize global error, a smooth contour with high accuracy can be obtained.

Considering that the BNNM with only one hidden layer is a general function approximator, it can approximate any continuous function. The input of the BNNM is the data sequence D, and the output layer consists of two units, corresponding to x and y, respectively. The Sigmoid function used as the activation function can be defined as $f_1(x) = 1/(1 + e^{-x})$ in the hidden layer, and the linear activation function $f_2(x) = x$ is used in the output layer. The smooth mathematical expression of lung ROI contour can be shown as,

$$f(t) = (x(p_i(x)), y(p_i(y))) = \left(\sum_{i=1}^{S}\left(\frac{1}{1+e^{-(t\omega_i - r_{1,i})}}\right) v_{i,1} - r_{2,1}, \sum_{i=1}^{S}\left(\frac{1}{1+e^{-(t\omega_i - r_{1,i})}}\right) v_{i,2} - r_{2,2}\right) \quad (3)$$

In formula (3), the lung ROI contour consists of the whole output points, where the points are denoted with coordinates. As can be seen, the coordinate x and y can be shown as the continuous function $x(p)$ and $y(p)$ on projection index p, respectively. We use the data sequence D consisting of the coordinate (x,y) and projection index p as the input of the BNNM, the smooth mathematical expression is firstly proposed by combination with theoretical and practical experiments through repeated attempts. The parameters of the BNNM are used to denote the smooth mathematical expression, where the parameters in formula (3) are expressed as follows,

S is the number of hidden units,

ω_i (i = 1, 2,. . ., S) is the weight from the input layer to the *i-th* hidden neuron,

$v_{i,k}$ (i = 1, 2 . . ., S; k = 1, 2) is the weight between the *i-th* hidden neuron and the *k-th* output neuron,

$r_{1,i}$(i = 1, 2,. . ., S) is the threshold of the *i-th* hidden neuron,

$r_{2,k}$ (k = 1, 2) is the threshold of the *k-th* output neuron.

III. EXPERIMENTAL RESULTS

In order to prove the universality of the proposed model, the private hospital database and the four public databases are used as the research object to evaluate the performance of the proposed algorithm. The four public datasets are the Japanese Society of Radiological Technology (JSRT) database [32]–[34], Montgomery County chest X-ray (MC) database, ShenZhen hospital Chest X-ray (SZCX) database [35] and OpenIST database, respectively. The private hospital database is used to select the optimal performance of the proposed method in detail (Section III-C). The quantitative and qualitative evaluations are used on the public JSRT database (Section III-D-1) to Section III-D-3)). Compared with the state-of-the-art methods, all four public databases are used (Section III-D-4)). All the ground truths are marked and verified by four professional radiologists. Each radiologist independently checks their own marks along with the anonymous marks of the other radiologists, and the consensus ground truth can be obtained by the majority voting of four experts' annotations. When the two markers have the same number of votes, radiologists will negotiate and try to reach consensus. All experiments presented here are done on a computer with Intel Core i7-8750H CPU and Geforce GTX 1070 GPU with 8GB memory.

A. DATABASE

We use five different databases for our experiment to evaluate the performance of our proposed method. TABLE 1 depicts the summary of several publicly available databases with major information, while the details of each dataset are presented below.

1) CLINICAL DATABASE

The clinical database is the anonymous chest X-ray database achieved in partnership with the 2nd Hospital of Soochow University. The CXR images are obtained by a Digital Radiography (DR) unit (Philips DigitalDiagnost C50) with high

Algorithm 3 Closed Polygonal Line Model(CPLM)

Input: initial segmentation result T achieved by the preprocessing step
Output: data sequences D (consist of T and the ordered projection indexes P)
Normalize the dataset T to the range {(-1,-1)~(1,1)}
Initialize the closed curve as the first principal component line
for i=1 to the dataset T do
  if($k>c\left(n,\Delta_n\left(f_{k,n}\right)\right)=\beta*n^{1/3}r*(\Delta_n(f_{k,n})^{-1/2})$;whole loop)
    if(outer loop constraint)
      if(constraint on the vertex, line segment, curve shape)
        if(inner loop constraint)
          projection step
          vertex optimization step
          k++
        else insert a new vertex
          update the position of each vertex
          adjust the shape of the curve
end for
Obtain a closed polygonal curve which consists of line segments
Project the dataset T to the closed polygonal curve
return data sequences D

>Normalization
>Initialization
>Stop condition
>Stop condition
>Constraint conditions
>Stop condition
>PLM
>PLM
>PLM
>PLM
>PLM
Improvement
Different from PLM
Traditional PLM

TABLE 1. Brief description of publicly available databases.

Database name	Year	Type	Attributes
JSRT database	2000	Public	Number of Images: 247 Medical Organs: Chest, Lung Image Type: IMG Image Resolution: 2048x2048 pixels
MC database	2014	Public	Number of Images: 138 Medical Organ: Chest (Frontal) Image Type: PNG Image Resolution: 4020x4892 or 4892x4020 pixels
SZCX database	2014	Public	Number of Images: 662 Medical Organ: Chest (Frontal) Image Type: PNG Image Resolution: 3000x3000 pixels
OpenIST database	2017	Public	Number of Images: 405 Medical Organs: Chest, Lung Image Type: JPG Image Resolution: 500x500 pixels

accuracy, which has a pixel size of 143 μm, a matrix of 2827 $\times$ 2823 pixels, and a panel size of 43 $\times$ 43cm. The exposure parameters are 125 kVp and 522-622 mA. The selected patients ranged in age from 18 to 66, with no pulmonary nodules. Considering the redundancy of the work, each patient takes only one slice in the postero-anterior view. Thereby, we randomly sample some patients and obtain the same number of slices, which the format is DICOM (DCM), then downsample to 512 $\times$ 512 for contour detection.

2) JSRT DATABASE

The JSRT database is one of the public databases for evaluating lung segmentation with chest radiographs, which is available more than a decade ago [32]. The JSRT database contains 247 chest radiographs, and it can be imported with the ImageJ software (https://imagej.nih.gov/ij/) offered by the JSRT official website. Each CXR image represented by the 12-bit gray-level image with the size of 2048 $\times$ 2048 pixels is in DCM file format. The JSRT database is the standard set of digital CXR images annotated by radiologists, and it is always used as a benchmark by many researchers to test their algorithms.

3) MC DATABASE

The standard digital image database is created by the Department of Health and Human Services of Montgomery County, Maryland, USA. This image dataset contains 138 posterior-anterior x-rays, where 58 are abnormal with different levels of tuberculosis manifestations and 80 are normal. All images are available in PNG format and the matrix size is 4020 $\times$ 4892 or 4892 $\times$ 4020 pixels. The dataset is publicly available on https://ceb.nlm.nih.gov/repositories/tuberculosis-chest-x-ray-image-data-sets/

4) SZCX DATABASE

The CXRs are collected in collaboration with Shenzhen No.3 People's Hospital, Guangdong Medical College, Shenzhen, China. The CXR images are from outpatient clinics and have been captured as part of the daily routine using a Philips DR digital diagnostic system. The set contains 662 images, where 326 are normal and 336 are abnormal with different levels of tuberculosis manifestations. All images are available in PNG format and the matrix size is 3000 × 3000 pixels. The dataset is publicly available on https://ceb.nlm.nih.gov/repositories/tuberculosis-chest-x-ray-image-data-sets/, and dataset description is publicly available in https://www.kaggle.com/yoctoman/shcxr-lung-mask

5) OPENIST DATABASE

This dataset contains 405 images, which are available in JPG format and the matrix size is 500 × 500 pixels. The dataset is publicly available on https://github.com/pi-null-mezon/OpenIST/tree/master/Datasets

B. EVALUATION METRICS

To prove the performance of the proposed hybrid method, several commonly criterions are considered for evaluation.

1) JACCARD SIMILARITY COEFFICIENT (Ω)/DICE SIMILARITY COEFFICIENT (DSC)

Ω is defined as the agreement between the manually delineated results by several professional radiologists called Ground Truth (*Gt*) and the segmentation results achieved by the proposed model called (*Auto*) [36], [37]. F1-score/Dice Similarity Coefficient (*DSC*) is often used to quantify the similarity between *Gt* and *Auto* [38], [39].

$$\Omega = \frac{|\mathrm{Gt} \cap \mathrm{Auto}|}{|\mathrm{GtUAuto}|} = \frac{|\mathrm{TP}|}{|\mathrm{FP}| + |\mathrm{TP}| + |\mathrm{FN}|} \tag{4}$$

$$\mathrm{DSC} = \frac{|\mathrm{Gt} \cap \mathrm{Auto}|}{|\mathrm{Gt}| + |\mathrm{Auto}|} = \frac{2\,|\mathrm{TP}|}{2\,|\mathrm{TP}| + |\mathrm{FP}| + |\mathrm{FN}|} \tag{5}$$

2) SENSITIVITY (SEN)/ POSITIVE PREDICTIVE VALUE (PPV)

Recall/Sensitivity (*Sen*) measures the portion of positive voxels in the *Gt* that is shown as positive by the segmentation being evaluated [40]. Precision/Positive Predictive Value (*PPV*) is used to evaluate the correctness of the segmentation region [41]. A value closer to 1 indicates a higher level of consistency.

$$\mathrm{Sen} = \frac{|\mathrm{Gt} \cap \mathrm{Auto}|}{|\mathrm{Gt}|} \tag{6}$$

$$\mathrm{PPV} = \frac{|\mathrm{Gt} \cap \mathrm{Auto}|}{|\mathrm{Auto}|} \tag{7}$$

Among them, True Positives (*TP*) denotes the correctly classified pixels. False Positives (*FP*) indicates the pixels that are classified as objects, which are actually background pixels. False Negatives (*FN*) shows the pixels which are classified as background but are actually objects.

3) GLOBAL ERROR (E) / MEAN SQUARE ERROR (MSE)

Global Error (E) is used to evaluate the convergence of the machine learning model [42], where E_k represents the deviation between the actual output y and the expected output c in the neural network is mean square error [43].

$$\mathrm{E} = \sum_{\mathrm{i}=1}^{\mathrm{N}} \mathrm{E_k} \tag{8}$$

$$\mathrm{E_k} = \frac{1}{\mathrm{N}} \sum\nolimits_{\mathrm{t}=1}^{\mathrm{N}} (\mathrm{y} - \mathrm{c})^2 \tag{9}$$

C. PERFORMANCE EVALUATION ON THE PRIVATE DATABASE

In this section, we use both the preprocessing step and the refinement step to analyze the experimental results in detail, then the optimal performance of the proposed Hull-CPLM can be chosen. We randomly choose 150 CXR images from the private hospital database as the research objects. The used 150 CXR images contain 85 males and 65 females, aged from 18 to 66 years, with a median age of 43 years and an average age of 48.15 years. The average results can be shown below.

1) PREPROCESSING

With the initial data points, the coarse segmentation can be achieved by the preprocessing step. TABLE 2 shows the different preprocessing results on different scale parameters s. We choose the *DSC*, Ω and execution time t as the evaluation parameters, where the s is changed from 10 to 40.

TABLE 2. The different prepocesssing results on different *s*.

	s=10	*s*=20	*s*=30	*s*=40
DSC	0.59	0.67	0.71	0.79
Ω	0.42	0.50	0.55	0.65
Execution Time *t* (s)	1.57	1.66	3.24	3.88

As shown in TABLE 2, for the specific database, under different s, the global trend of the preprocessing step is that the *DSC* and Ω are increasing with the s. However, when the s is 10, too small s will lead to obtaining too few true positive points. When the s changes from 20 to 30, the *DSC* and Ω increases slightly about 5.9% and 10%, respectively, while the consumed execution time (t) increases about 95.1%. It can be seen that if the scale parameter is too large, too many unused points will be added and more execution time will cost, so we use $s = 20$.

Overall, TABLE 2 shows that the Hull model in the preprocessing stage is used to obtain the convex-concave contour of the initial dataset. To ensure that the proposed model is suitable for different shapes of the initial input, and achieve higher precision, we can further correct the contour of the lung ROI by the refinement step.

2) REFINEMENT STEP

After the preprocessing segmentation, we apply a refinement step consisting of the CPLM and the BNNM to locate the

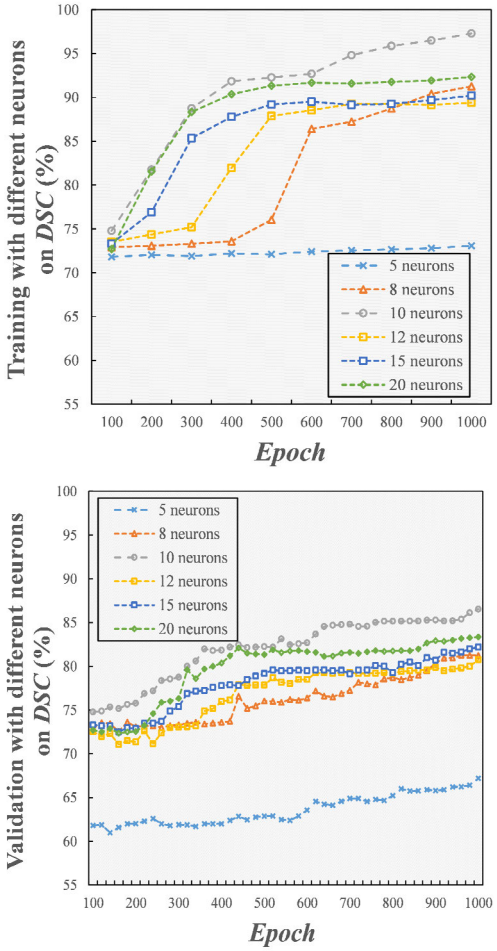

FIGURE 5. Comparison in DSC with different neurons on train data (left) and validation data (right).

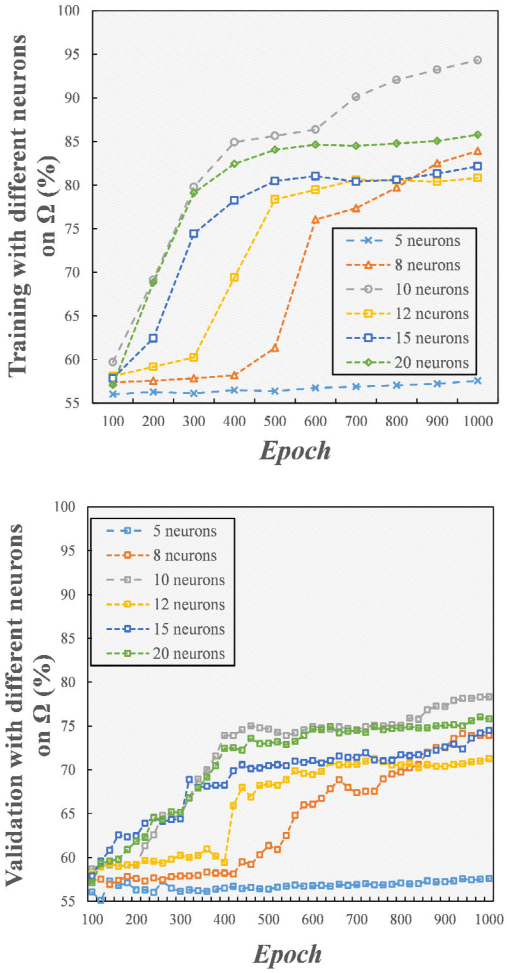

FIGURE 6. Comparison in Ω with different neurons on train data (left) and validation data (right).

lung borders more accurately. The 150 preprocessed results are used for evaluation, where 125 of them are used for training and 25 for validation. We train the BNNM using the same hyper-parameters as in [31]. We have further split the training set into five subsets, and we train on all subsets. The validation set is used to select an appropriate number of neurons for the BNNM and to choose the optimal model. The hyper-parameter neurons in BNNM varies in {5, 8, 10, 12, 15, and 20}. The BNNM is trained using a momentum parameter $= 1$ and learning rate $= 0.4$. From FIGURE 5 to FIGURE 10, the quantitative experimental results of the *DSC*, Ω, *Sen*, *PPV*, *E*, and *MSE* under different hidden neurons. We display the evolution of precision on the train and validation sets, where the left and right figures show the training and validation precision, respectively. Combining with the whole training and validation figures, we can see that the optimal model is selected with 10 neurons.

About the training figures, as illustrated from FIGURE 5 to FIGURE 8, with the increasing epochs, the *DSC*, Ω, *Sen*, and *PPV* are always increasing. When the epochs are 1000, the max *DSC*, Ω, *Sen*, and *PPV* can be obtained where the neurons are 10. Compared with the second comprehensive performance that the neurons are 20, the *DSC*, Ω, *Sen*, and *PPV* increased by 5.34%, 9.95%, 5.12%, and 5.26%, respectively. When the neurons are 5, the *DSC*, Ω, *Sen*, and *PPV* are the smallest. The others have a similar trend in the evaluation parameters.

When the epochs change from 800 to 1000, the *DSC*, Ω, *Sen*, and *PPV* decrease slightly and then rise again, when the hidden neurons are selected as 12 and 15, respectively. The evaluation parameters do not rise but decrease with the increasing epochs, and the overfitting is caused. The main reason for the overfitting is the model contains too many parameters, which makes the model complicated. However, the machine learning model has the ability to resist the overfitting, the evaluation parameters continue to increase after slightly dropping. The *E* and *MSE* are also used for the selection of optimal performance of the proposed model. As shown From FIGURE 9 and FIGURE 10, the *E* and *MSE* have similar trends. The *E* and *MSE* are always decreasing and stabled eventually. Among all, the 5 neurons have the highest *E* and *MSE*, which are around 0.048 and 0.87×10^{-6},

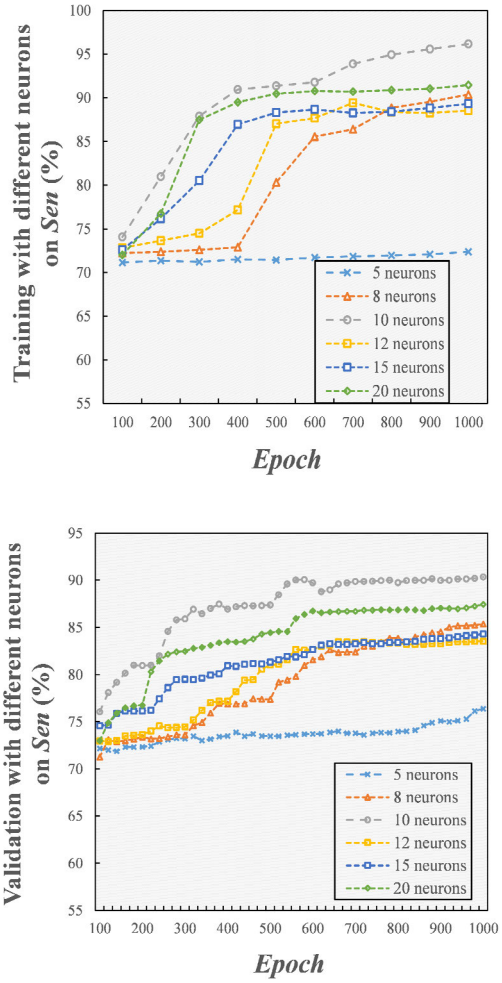

FIGURE 7. Comparison in *Sen* with different neurons on train data (left) and validation data (right).

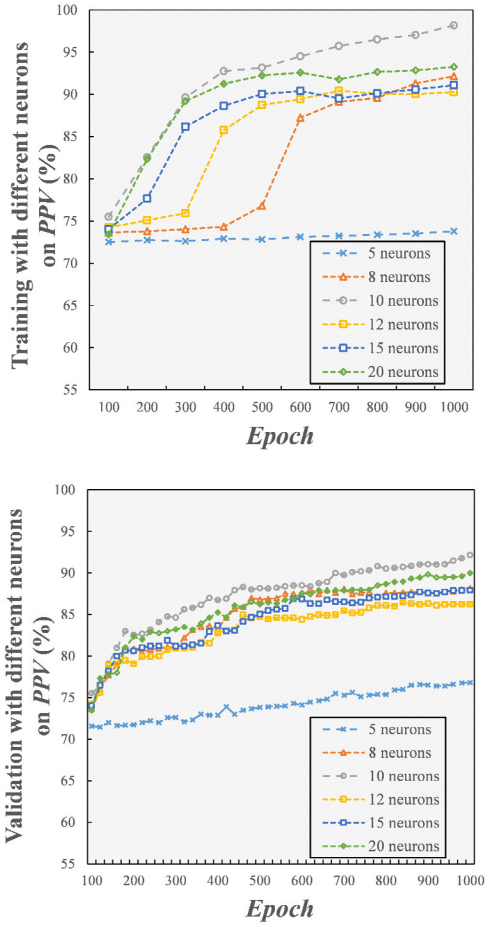

FIGURE 8. Comparison in *PPV* with different neurons on train data (left) and validation data (right).

respectively. The E and MSE of the others eventually fall below 0.03 and 0.58×10^{-6}, respectively.

D. PERFORMANCE EVALUATION ON THE PUBLIC DATABASES

Based on the selected optimal model in the previous section, we test the model on public datasets. In this section, we use four public databases for experiments. The public JSRT database is used for quantitatively and qualitatively performance assessment in Section III-D-1) to Section III-D-3), where 93 images are normal images and 154 are nodule-containing images. The whole four public databases are used for quantitative comparison with the state-of-the-art methods in Section III-D-4).

1) COMPARISON WITH MULTI-RESOLUTION IMAGES ON PUBLIC JSRT DATABASE

TABLE 3 shows the performance of the proposed Hull-CPLM using the *DSC* and Ω as the evaluation metrics on various resolutions, where whole (All), negative (-), and positive (+) cases denote the whole dataset, non-nodule, and the nodule radiographs, respectively. From the public JSRT database containing 247 images, the training and testing images of the All, −, + cases are 167 and 80 images, 63 and 30 images, 104 and 50 images, respectively. From TABLE 3, based on the CXR images, the proposed model can obtain the *DSC* above 0.9 for all CXR images within the public JSRT database with an average *DSC* of 0.958 for all resolutions. These *DSC* values show that compared with the falsely segmented regions, the true positive pixels inside the resulting lung ROI can describe the real contour of the dataset more significant.

For all CXR images, the Ω obtained by the proposed method can reach more than 0.85, while the average Ω is 0.92 for all resolutions; so making superior or inferior areas of lung ROI contour are incorrectly extracted whether caused by either false positive or negative pixels. Considering the degree of detail of the CXR images, segmentation performance is opposite with the change of image resolution. Most of these details are always corresponding to the intermediate textures, and most segmentation models cannot segment them accurately.

According to TABLE 3, we can see that there is only a slight deviation between the *DSC* and Ω in each case,

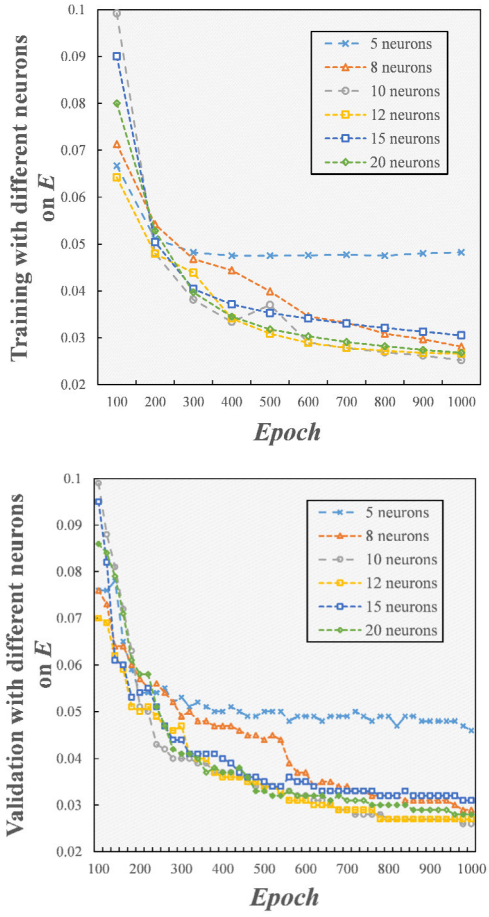

FIGURE 9. Comparison in *E* with different neurons on train data (left) and validation data (right).

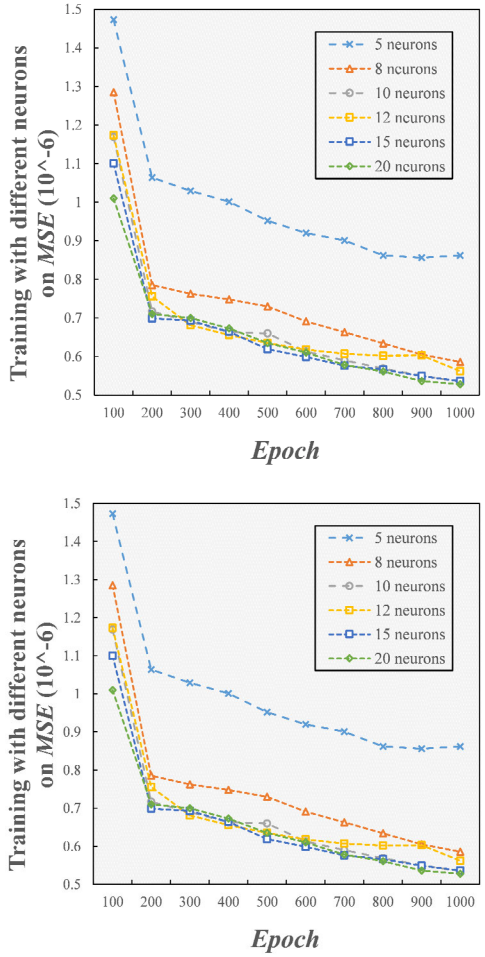

FIGURE 10. Comparison in *MSE* with different neurons on train data (left) and validation data (right).

TABLE 3. Precision of the proposed method using the *DSC* and Ω on various resolutions (*DSC* and Ω in mean + standard deviation).

Resolution	Case	*DSC*	Ω
256x256	All	0.965±0.011	0.932±0.018
	-	0.963±0.011	0.928±0.018
	+	0.967±0.010	0.936±0.017
512x512	All	0.962±0.012	0.926±0.019
	-	0.958±0.010	0.919±0.019
	+	0.963±0.012	0.928±0.020
1024x1024	All	0.949±0.011	0.903±0.021
	-	0.948±0.009	0.901±0.021
	+	0.952±0.011	0.908±0.020

which proves that the proposed method is not affected too much whether the CXR images contain nodules. When the resolution of all CXR images is 256 × 256, the optimal *DSC* and Ω are 0.965 ± 0.011 and 0.932 ± 0.018, respectively.

2) COMPARISON WITH DIFFERENT HYBRID METHODS ON PUBLIC JSRT DATABASE

In this section, we randomly select three CXR images of the non-nodule group from public JSRT and compare with different hybrid methods globally. Then the costophrenic angle and apical region of each global results are partial magnification for comparison. According to the experimental analysis in the previous section, all of the original radiographs are downsampled into 256 × 256 to be compatible with published results.

a: GLOBAL COMPARISON

For experimental analysis, we use the hybrid CPLM-BNNM and Deep Belief Network Model-K-Nearest Neighbor Method (DBNM-KNNM) as the compared models. Among them, all three models use as low as 15% of the manual points to be initial points. Through repeated training, the optimal results of each model are selected, while quantitative and qualitative analysis is assisted with some evaluation metrics. Considering that CPLM-BNNM has optimal performance settings, we set hidden neurons to 10 [31]. In order to comprehensively consider the overall performance of the DBNM-KNNM, such as time complexity and precision of the model, the DBNM is eventually set up to contain two hidden layers, each containing 25 and 30 neurons. FIGURE 11 shows the global segmentation results obtained by different hybrid methods, where the red lines show the *Gt* and blue lines show the *Auto*.

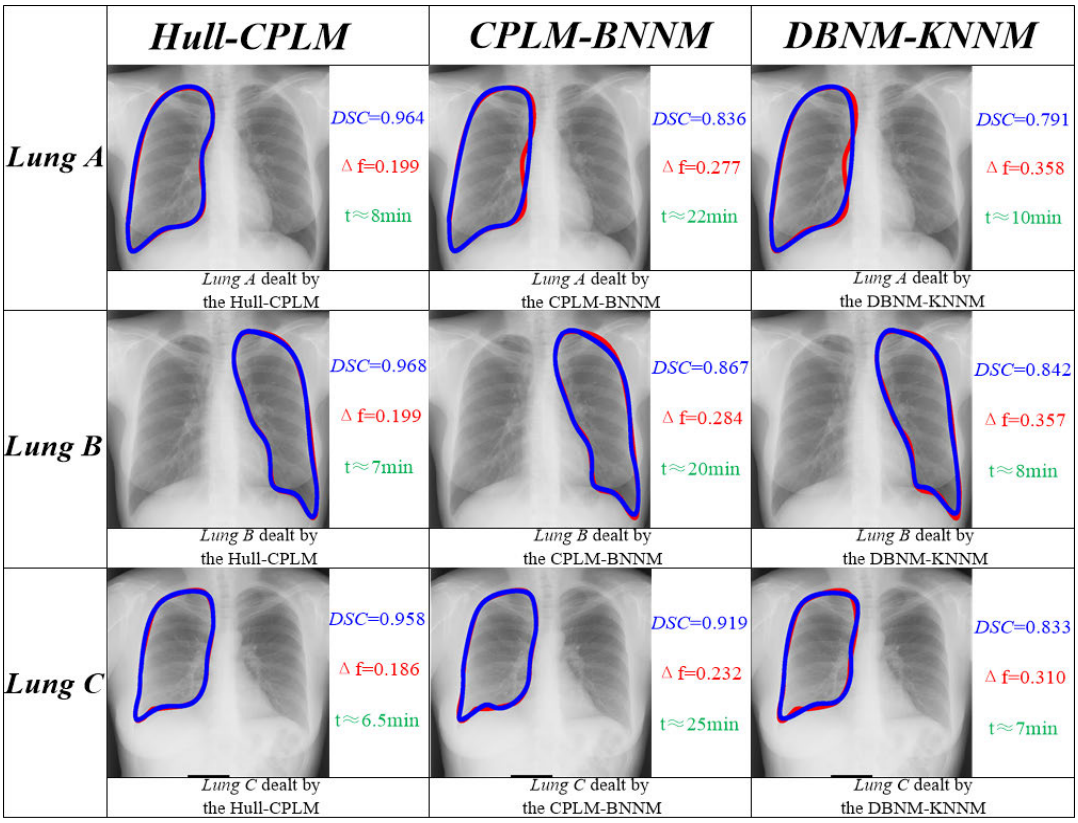

FIGURE 11. Global comparison with different hybrid methods.

The *DSC*, Δf and execution time t are used for evaluating the performance of all three models (see FIGURE 11), where Δf denotes the global Euclidean square distance function [44]. In principle, if Δf is smaller, the curve f is closer to the real distribution of dataset, and it means that the obtained results have higher precision. Compared with the CPLM-BNNM which has the second comprehensive performance, the *DSC* and Δf of the Hull-CPLM increases as high as 15.3% and decreases as low as 42.7%, respectively, while t consumes only about 30%. Compared with the DBNM-KNNM, the CPLM-BNNM has better *DSC* and Δf, while it needs more time for training. It denotes that deep learning model has a much more complex network model and can fit the dataset faster, while the limited initial dataset restricts the fitting precision.

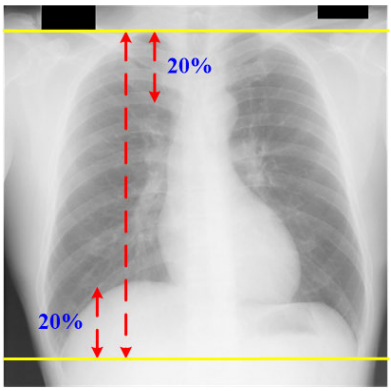

FIGURE 12. Segmenting the AR and CPR. These regions correspond approximately to thetop 20% and bottom 20% of the lung.

b: PARTIAL MAGNIFICATION OF COSTOPHRENIC ANGLE AND APICAL REGIONS

In order to preserve the important regions of the lung boundary such as Apical Regions (AR) and CostoPhrenic angle Regions (CPR), accurate segmentation of these regions is very necessary [45]. CostoPhrenic (CP) angle blunting is usually considered to represent abnormal pulmonary [46]. However, compared with the other parts of the lung, these regions segmentation is more challenging because of the small CP angle. In order to quantitatively and qualitatively compare the performance of all three hybrid methods for these regions, we use the top 20% and bottom 20% of the lung as the research object which is the partial magnification of the global comparison results in FIGURE 11, as shown in FIGURE 12 and FIGURE 13.

For more accurate experimental analysis, we use both the *DSC* and Ω to evaluate the precision of the extracted AR and CPR. According to FIGURE 13, the proposed method can segment most regions of both the AR and CPR of the chest radiography. Compared with the CPLM-BNNM and

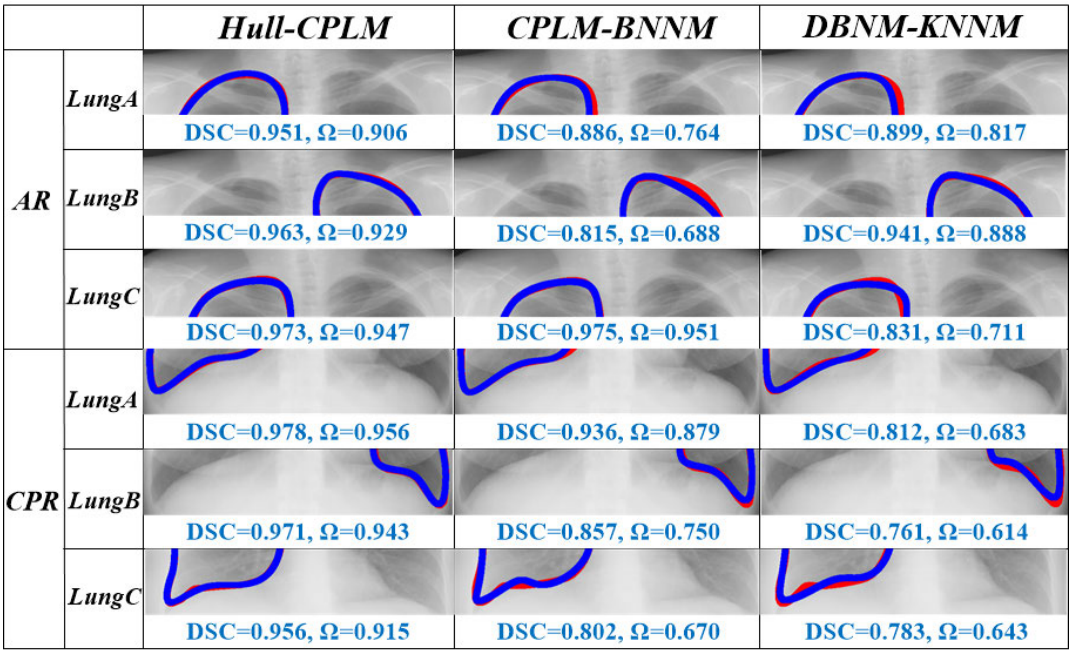

FIGURE 13. Partial magnification of the AR and CPR.

DBNM-KNNM, the performance of the proposed method in lung segmentation is the most stable, and it can obtain better segmentation precision.

3) COMPARISON WITH STATE-OF-THE-ART METHODS ON PUBLIC JSRT DATABASE

By means of the previous experiments, we have demonstrated that the proposed model is both effective and efficient for lung segmentation. To validate the performance of our model, we compare our models with state-of-the-art methods on the public JSRT database. Considering that the machine learning model is always affected by the overfitting, we choose to simplify the complex network model and set the number of neurons is 10 to avoid overfitting. The optimal experimental results are obtained by the proposed model where the epoch is 1200 (corresponding execution time is about 10min). All of the JSRT images are utilized and Ω is treated as the evaluation criterion, where the mean value of Ω and the Standard deviation value (Std) value of Ω are used to evaluate the precision and stability of the method, respectively. To be more intuitive, FIGURE 14 and TABLE 4 are used to show the comparison between our method and other existing methods in literature in terms of the mean value of Ω and the Std of Ω, respectively, where the proposed result shown in FIGURE 14 is the average value obtained by repeated experiments.

- Machine learning model (Ref. [49], [51]–[53]): Coppini *et al*. [49] built with a neural network architecture to implement lung fields segmentation exploiting image features and prior knowledge, while Kaur *et al*. [51] and Neff *et al*. [52] proposed a Deep Convolutional Neural Network (DCNN) and a new variant of Generative Adversarial Networks (GANs) for lung segmentation in chest radiographs, respectively. The Ω of each model is 0.927 ± 0.033, 0.934, and 0.924, respectively. Novikov *et al*. [53] presented a Fully Convolutional Neural Network (FCNN) to complete lung segmentation on public JSRT, and the Ω is as high as 0.95.

  Note that in Ref. [52], the authors only use average *DSC* to evaluate the performance of the method. For a comprehensive comparison, we use the transform formula [49], [54] to calculate another metric and labeled the results with "$*$".

- Hybrid model (Ref. [47], [48], [50]): Yu *et al*. [47] reported the performance of the hybrid Shape Regularized Active Contour model (ShRAC) on 247 CXR images from JSRT database. Shi *et al*. [48] presented a hybrid model using both population-based and patient-specific shape statistics to segment lung fields from serial chest radiographs, while Li *et al*. [50] proposed an automatic lung field segmentation method for X-ray radiographs using Statistical Shape Model (SSM) and Appearance Model (SAM). All three models use the public JSRT database to prove the performance and obtain the Ω of 0.907 ± 0.033, 0.920 ± 0.031, and 0.931 ± 0.019, respectively.

According to FIGURE 14 and TABLE 4, the proposed method obtains a higher Ω and the standard deviation than other methods to prove the better precision and stability, respectively, except for Ref. [51] and Ref. [53]. In Ref. [51] and Ref. [53], both of them do not use the standard deviation of the Ω to evaluate the stability of the methods. Speed as an essential parameter is always used for proving

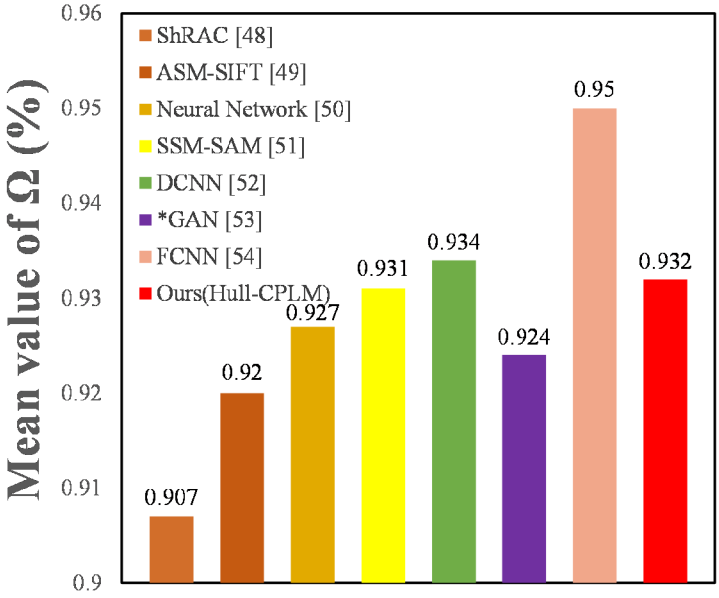

FIGURE 14. The performance comparison with the mean value of Ω on public JSRT.

TABLE 4. The performance comparison with the Std of Ω on public JSRT. (* denotes the conversation result).

Reference	Method	Model	Database	Images (used/total)	Std of Ω
[48]-2005	ShRAC	Hybrid	JSRT	247/247	0.033
[49]-2008	ASM-SIFT	Hybrid	JSRT	247/247	0.031
[50]-2013	Neural Network	Machine learning	JSRT	247/247	0.033
[51]-2016	SSM-SAM	Hybrid	JSRT	247/247	0.019
[52]-2017	DCNN	Machine learning	JSRT	247/247	N/A
[53]-2017	*GAN	Machine learning	JSRT	247/247	N/A
[54]-2018	FCNN	Machine learning	JSRT	247/247	N/A
Proposed method	**Hull-CPLM**	**Hybrid**	**JSRT**	**247/247**	**0.018**

the performance of the models. Among the three methods, Ref. [51] does not use speed as an evaluation metric, so we only compare Ref. [53] with our proposed method.

From FIGURE 14, it is clear that the method proposed by Novikov *et al.* [53] achieves Jaccard values of around 95% on JSRT, which is higher than our proposed method. However, training time for their models takes at least 12.4 hours, while ours have only used about 10 minutes to obtain the final result. Novikov *et al.* [53] performed all the experiments on a PC with Intel Xeon CPU E5-2650 v3 @ 2.30 GHz and GeForce GTX TitanX GPU with 12 GB memory. Compared with them, we have only used Intel Core i7-8750H CPU @ 2.20GHz and GeForce GTX 1070 with 8 GB memory. Compared with their GPU,[1] the performance of our GPU[2] is much lower (∼40% lower). The training time of our method is faster compared with Novikov, making our method more suitable for resource-constrained systems.

[1]https://en.wikipedia.org/wiki/GeForce_900_series
[2]https://en.wikipedia.org/wiki/GeForce_10_series

4) COMPARISON WITH STATE-OF-THE-ART METHODS ON FOUR PUBLIC DATABASES

Evaluation measures can be classified based on two approaches: region-based and boundary-based metrics [55], where Ω we have used is one of the region-based metrics. Therefore, we will use a boundary-based metric called accuracy *(ACC)* to assess the accuracy of the method. In order to evaluate the performance of the proposed method more comprehensively, we use four publicly available databases as research objects, where the *ACC* is used. The *ACC* is computed as,

$$\mathrm{ACC} = \frac{|\mathrm{TP}| + |\mathrm{TN}|}{|\mathrm{TP}| + |\mathrm{FN}| + |\mathrm{FP}| + |\mathrm{TN}|} \tag{10}$$

• Machine learning model (Ref. [56]): Rashid et al. [56] presented with a deep fully convolutional neural network architecture for lung segmentation from CXR images. The ACC of the models is as high as 0.97 and 0.97 for JSRT database and MC database, respectively.

• Hybrid model (Ref. [57], [58]): Vajda et al. [57] proposed a hybrid model using both feature selection strategy and

TABLE 5. The performance comparison with the *ACC* on four public databases.

Reference	Method	Model	Database	*ACC*
[56]-2018	FCNN	Machine learning	JSRT/MC	0.97/0.97
[57]-2018	Feature Selection strategy and Neural Network	Hybrid	MC/SZCX	0.69/0.92
[58]-2018	Feature selection and BN	Hybrid	MC/SZCX	0.77/0.81
[58]-2018	Feature selection and MLP	Hybrid	MC/SZCX	0.79/0.88
[58]-2018	Feature selection and RF	Hybrid	MC/SZCX	0.81/0.89
[58]-2018	Feature selection and Vote(BN, MLP, RF)	Hybrid	MC/SZCX	0.83/0.91
Proposed method	**Hull-CPLM**	**Hybrid**	**JSRT/MC/SZCZ/OpenIST**	**0.97/0.97/0.97/0.97**

neural network to segment lung fields, where *ACC* is used for the different feature representations for different data collections. It is noteworthy that the majority of the CXR images in the MC database have more tuberculosis manifestations inside the lung regions, therefore it can lead to severe shape deformations. The ACC of the models is 0.69 and 0.92 for MC database and SZCX database, respectively.

Santosh et al. [58] firstly obtained the shape features of lung region using the local and global representation of the lung regions, and then different classifiers are used for classification. The classifiers are the Bayesian Network (BN), Multi-Layer Perception neural networks (MLP), Random Forest (RF), and voting-based combination of three different classifiers (Vote (BN, MLP, RF)), respectively. The different hybrid methods are tested on the MC database and SZCX database, respectively, while the ACCs of these methods are 0.77/0.81, 0.79/0.88, 0.81/0.89, and 0.83/0.91, respectively.

According to TABLE 5, the proposed method achieved the same or higher ACC compared with other methods. Although the ACCs in [56] are the same for both JSRT and MC databases compared with the proposed Hull-CPLM, the DSC (0.951) is not as good as that of the proposed method (0.965).

IV. CONCLUSION

We have presented a semi-automatic model for lung segmentation called the Hull-CPLM. The core of our technique is to improve segmentation accuracy by integrating several newest technologies. Only about 15% of the manually delineated points provided by clinicians is used as the initial points. The preprocessing step uses the Hull consisting of the CHM and the CCHM to implement the coarse segmentation. In the refinement stage, the CPLM-BNNM is mainly used to refine the results and obtain a unified and smooth mathematical expression of the lung ROI contour. The effectiveness and the robustness of our proposed model are tested with the private clinical database and four public databases. The performance of the proposed method is evaluated quantitatively and qualitatively by comparing with different shape-based segmentation models using different evaluation metrics, while compared with the state-of-the-art methods on four public databases, demonstrating promising results. We want to further reduce the training time of the proposed machine learning model, and we plan to test the proposed model on other organs.

REFERENCES

[1] J. L. López-Campos, W. Tan, and J. B. Soriano, "Global burden of COPD," *Respirology*, vol. 21, no. 1, pp. 14–23, Jan. 2016.
[2] I. Nardi-Agmon, M. Abud-Hawa, O. Liran, N. Gai-Mor, M. Ilouze, A. Onn, J. Bar, D. Shlomi, H. Haick, and N. Peled, "Exhaled breath analysis for monitoring response to treatment in advanced lung cancer," *J. Thoracic Oncol.*, vol. 11, no. 6, pp. 827–837, Jun. 2016.
[3] W.-L. Lee, K. Chang, and K.-S. Hsieh, "Unsupervised segmentation of lung fields in chest radiographs using multiresolution fractal feature vector and deformable models," *Med. Biol. Eng. Comput.*, vol. 54, no. 9, pp. 1409–1422, Sep. 2016.
[4] J. C. Souza, J. O. B. Diniz, J. L. Ferreira, G. L. F. da Silva, A. C. Silva, and A. C. de Paiva, "An automatic method for lung segmentation and reconstruction in chest X-ray using deep neural networks," *Comput. Meth. Programs Biomed.*, vol. 177, pp. 285–296, Aug. 2019.
[5] A. Mittal, R. Hooda, and S. Sofat, "LF-SegNet: A fully convolutional encoder–decoder network for segmenting lung fields from chest radiographs," *Wireless Pers. Commun.*, vol. 101, no. 1, pp. 511–529, Jul. 2018.
[6] R. Hooda, A. Mittal, and S. Sofat, "An efficient variant of fully-convolutional network for segmenting lung fields from chest radiographs," *Wireless. Pers. Commun.*, vol. 101, no. 3, pp. 1559–1579, Aug. 2018.
[7] M. Khened, V. A. Kollerathu, and G. Krishnamurthi, "Fully convolutional multi-scale residual DenseNets for cardiac segmentation and automated cardiac diagnosis using ensemble of classifiers," *Med. Image. Anal.*, vol. 1, no. 51, pp. 21–45, Jan. 2019.
[8] K. C. L. Wong, T. Syeda-Mahmood, and M. Moradi, "Building medical image classifiers with very limited data using segmentation networks," *Med. Image. Anal.*, vol. 1, no. 49, pp. 105–116, Oct. 2018.
[9] P. Lakhani and B. Sundaram, "Deep learning at chest radiography: Automated classification of pulmonary tuberculosis by using convolutional neural networks," *Radiology*, vol. 284, no. 2, pp. 574–582, Aug. 2017.
[10] Z. Fan, J. Lu, C. Wei, H. Huang, X. Cai, and X. Chen, "A hierarchical image matting model for blood vessel segmentation in fundus images," *IEEE Trans. Image Process.*, vol. 28, no. 5, pp. 2367–2377, May 2019.
[11] D. S. Jodas, A. S. Pereira, and J. M. R. S. Tavares, "Automatic segmentation of the lumen region in intravascular images of the coronary artery," *Med. Image. Anal.*, vol. 40, pp. 60–79, Aug. 2017.
[12] E. Ilunga-Mbuyamba, J. G. Avina-Cervantes, A. Garcia-Perez, R. de Jesus Romero-Troncoso, H. Aguirre-Ramos, I. Cruz-Aceves, and C. Chalopin, "Localized active contour model with background intensity compensation applied on automatic MR brain tumor segmentation," *Neurocomputing*, vol. 220, pp. 84–97, Jan. 2017.
[13] A. A. Kiaei and H. Khotanlou, "Segmentation of medical images using mean value guided contour," *Med. Image. Anal.*, vol. 40, pp. 111–132, Aug. 2017.

[14] S. Shen, A. A. T. Bui, J. Cong, and W. Hsu, "An automated lung segmentation approach using bidirectional chain codes to improve nodule detection accuracy," *Comput. Biol. Med.*, vol. 57, pp. 139–149, Feb. 2015.

[15] W. S. H. M. W. Ahmad, W. M. D. W. Zaki, and M. F. A. Fauzi, "Lung segmentation on standard and mobile chest radiographs using oriented Gaussian derivatives filter," *Biomed. Eng. Online.*, vol. 14, Mar. 2015, Art. no. 20.

[16] A. Pratondo, C.-K. Chui, and S.-H. Ong, "Integrating machine learning with region-based active contour models in medical image segmentation," *J. Vis. Commun. Image Represent.*, vol. 43, pp. 1–9, Feb. 2017.

[17] H. Isack, O. Veksler, M. Sonka, and Y. Boykov, "Hedgehog shape priors for multi-object segmentation," in *Proc. 29th IEEE Conf. Comput. Vis. Pattern Recognit. (CVPR)*, Las Vegas, NV, USA, Jun. 2016, pp. 2434–2442.

[18] N. Tong, S. Gou, S. Yang, D. Ruan, and K. Sheng, "Fully automatic multi-organ segmentation for head and neck cancer radiotherapy using shape representation model constrained fully convolutional neural networks," *Med. Phys.*, vol. 45, no. 10, pp. 4558–4567, Oct. 2018.

[19] C. Shi, Y. Cheng, F. Liu, Y. Wang, J. Bai, and S. Tamura, "A hierarchical local region-based sparse shape composition for liver segmentation in CT scans," *Pattern Recognit.*, vol. 50, pp. 88–106, Feb. 2016.

[20] Z. Li, Y. Zhang, H. Gong, G. Liu, W. Li, and X. Tang, "An automatic and efficient coronary arteries extraction method in CT angiographies," *Biomed. Signal Process. Control*, vol. 36, pp. 221–233, Jul. 2017.

[21] B. Kegl and A. Krzyzak, "Piecewise linear skeletonization using principal curves," *IEEE Trans. Pattern Anal. Mach. Intell.*, vol. 24, no. 1, pp. 59–74, Jan. 2002.

[22] L. Khedher, J. Ramírez, J. M. Górriz, A. Brahim, and F. Segovia, "Early diagnosis of Alzheimer's disease based on partial least squares, principal component analysis and support vector machine using segmented MRI images," *Neurocomputing*, vol. 151, pp. 139–150, Mar. 2015.

[23] Z. Li, Y. Zhang, G. Liu, H. Shao, W. Li, and X. Tang, "A robust coronary artery identification and centerline extraction method in angiographies," *Biomed. Signal Process. Control*, vol. 16, pp. 1–8, Feb. 2015.

[24] Q. Wang, Y. Zheng, G. Yang, W. Jin, X. Chen, and Y. Yin, "Multiscale rotation-invariant convolutional neural networks for lung texture classification," *IEEE J. Biomed. Health Inform.*, vol. 22, no. 1, pp. 184–195, Jan. 2018.

[25] Y. Rong, D. Xiang, W. Zhu, K. Yu, F. Shi, Z. Fan, and X. Chen, "Surrogate-assisted retinal OCT image classification based on convolutional neural networks," *IEEE J. Biomed. Health Inform.*, vol. 23, no. 1, pp. 253–263, Jan. 2019.

[26] M. Bisele, M. Bencsik, M. G. C. Lewis, and C. T. Barnett, "Optimisation of a machine learning algorithm in human locomotion using principal component and discriminant function analyses," *PLoS ONE*, vol. 12, no. 9, Sep. 2017, Art. no. e0183990.

[27] R. L. Graham, "An efficient algorithm for determining the convex hull of a finite planar set," *Inf. Process. Lett.*, vol. 1, no. 4, pp. 132–133, 1972.

[28] A. L. Chau, X. Li, and W. Yu, "Convex and concave hulls for classification with support vector machine," *Neurocomputing*, vol. 122, pp. 198–209, Dec. 2013.

[29] T. Hastie and W. Stuetzle, "Principal curves," *J. Amer. Stat. Assoc.*, vol. 84, no. 406, pp. 502–516, 1989.

[30] B. Kégl, A. Krzyzak, T. Linder, and K. Zeger, "Learning and design of principal curves," *IEEE Trans. Pattern Anal. Mach. Intell.*, vol. 22, no. 3, pp. 281–297, Mar. 2000.

[31] T. Peng, Y. Wang, T. C. Xu, L. Shi, J. Jiang, and S. Zhu, "Detection of lung contour with closed principal curve and machine learning," *J. Digit. Imag.*, vol. 31, no. 4, pp. 520–533, Aug. 2018.

[32] K.-I. Komatsu, J. Ikezoe, M. Matsui, K. Doi, J. Shiraishi, H. Fujita, Y. Kodera, S. Katsuragawa, T. Kobayashi, and T. Matsumoto, "Development of a digital image database for chest radiographs with and without a lung nodule: Receiver operating characteristic analysis of radiologists' detection of pulmonary nodules," *Amer. J. Roentgenol.*, vol. 174, no. 1, pp. 71–74, Jan. 2000.

[33] W. Dai, N. Dong, Z. Wang, X. Liang, H. Zhang, and E. P. Xing, "SCAN: Structure correcting adversarial network for organ segmentation in chest X-rays," in *Deep Learning in Medical Image Analysis and Multimodal Learning for Clinical Decision Support—DLMIA*. Granada, Spain: Springer, 2018, pp. 263–273.

[34] B. van Ginneken, M. B. Stegmann, and M. Loog, "Segmentation of anatomical structures in chest radiographs using supervised methods: A comparative study on a public database," *Med. Image. Anal.*, vol. 10, no. 1, pp. 19–40, Feb. 2006.

[35] S. Jaeger, "Two public chest X-ray datasets for computer-aided screening of pulmonary diseases," *Quant. Imag. Med. Surg.*, vol. 4, no. 6, pp. 475–477, Dec. 2014.

[36] A. V. Nasrulloh, C. G. Willcocks, P. T. G. Jackson, C. Geenen, M. S. Habib, D. H. W. Steel, and B. Obara, "Multi-scale segmentation and surface fitting for measuring 3-D macular holes," *IEEE Trans. Med. Imag.*, vol. 37, no. 2, pp. 580–589, Feb. 2018.

[37] L. Bi, J. Kim, E. Ahn, A. Kumar, M. Fulham, and D. Feng, "Dermoscopic image segmentation via multistage fully convolutional networks," *IEEE Trans. Biomed. Eng.*, vol. 64, no. 9, pp. 2065–2074, Sep. 2017.

[38] M. Fu, W. Wu, X. Hong, Q. Liu, J. Jiang, Y. Ou, Y. Zhao, and X. Gong, "Hierarchical combinatorial deep learning architecture for pancreas segmentation of medical computed tomography cancer images," *BMC. Syst. Biol.*, vol. 12, no. 4, Apr. 2018, Art. no. 56.

[39] C. S. Perone, E. Calabrese, and J. Cohen-Adad, "Spinal cord gray matter segmentation using deep dilated convolutions," *Sci. Rep.*, vol. 8, no. 1, Apr. 2018, Art. no. 5966.

[40] A. A. Taha and A. Hanbury, "Metrics for evaluating 3D medical image segmentation: Analysis, selection, and tool," *BMC Med. Imag.*, vol. 15, no. 1, p. 29, 2015.

[41] L. Chen, Z. Zhou, and J. Wang, "SU-C-207B-03: A geometrical constrained Chan-Vese based tumor segmentation scheme for PET," *Med. Phys.*, vol. 43, no. 6, p. 3330, Jun. 2016.

[42] R. Rodriguez, O. O. V. Villegas, V. G. C. Sanchez, J. Bila, and A. Mexicano, "Arrhythmia disease classification using a higher-order neural unit," in *Proc. 4th Int. Conf. Future Gener. Commun. Technol. (FGCT)*, Luton, U.K., Jul. 2015, pp. 1–6.

[43] N. E. Krasowski, T. Beier, G. W. Knott, U. Köthe, F. A. Hamprecht, and A. Kreshuk, "Neuron segmentation with high-level biological priors," *IEEE Trans. Med. Imag.*, vol. 37, no. 4, pp. 829–839, Apr. 2018.

[44] L. Vincent, "Exact Euclidean distance function by chain propagations," in *Proc. IEEE Comput. Soc. Conf. Comput. Vis. Pattern Recognit. (CVPR)*, Maui, HI, USA, Jun. 1991, pp. 520–525.

[45] S. Candemir, S. Jaeger, K. Palaniappan, J. P. Musco, R. K. Singh, Z. Xue, A. Karargyris, S. Antani, G. Thoma, and C. J. McDonald, "Lung segmentation in chest radiographs using anatomical atlases with nonrigid registration," *IEEE Trans. Med. Imag.*, vol. 33, no. 2, pp. 577–590, Feb. 2013.

[46] P. Maduskar, L. Hogeweg, R. Philipsen, and B. van Ginneken, "Automated localization of costophrenic recesses and costophrenic angle measurement on frontal chest radiographs," *Proc. SPIE*, vol. 8670, Mar. 2013, Art. no. 867038.

[47] T. Yu, J. Luo, and N. Ahuja, "Shape regularized active contour using iterative global search and local optimization," in *Proc. IEEE Comput. Soc. Conf. Comput. Vis. Pattern Recognit. (CVPR)*, San Diego, CA, USA, Jun. 2005, pp. 655–662.

[48] Y. Shi, F. Qi, Z. Xue, L. Chen, K. Ito, H. Matsuo, and D. Shen, "Segmenting lung fields in serial chest radiographs using both population-based and patient-specific shape statistics," *IEEE Trans. Med. Imag.*, vol. 27, no. 4, pp. 481–494, Apr. 2008.

[49] G. Coppini, M. Miniati, S. Monti, M. Paterni, R. Favilla, and E. M. Ferdeghini, "A computer-aided diagnosis approach for emphysema recognition in chest radiography," *Med. Eng. Phys.*, vol. 35, no. 1, pp. 63–73, Jan. 2013.

[50] X. Li, S. Luo, Q. Hu, J. Li, D. Wang, and F. Chiong, "Automatic lung field segmentation in X-ray radiographs using statistical shape and appearance models," *J. Med. Imag. Health Inform.*, vol. 6, no. 2, pp. 338–348, Apr. 2016.

[51] S. Kaur, R. Hooda, A. Mittal, and S. Sofat, "Deep CNN-based method for segmenting lung fields in digital chest radiographs," in *Proc. Int. Conf. Adv. Inform. Comput. Res.*, Singapore, 2017, pp. 185–194.

[52] T. Neff, C. Payer, D. Štern, and M. Urschler, "Generative adversarial network based synthesis for supervised medical image segmentation," in *Proc. OAGM ARW Joint Workshop*, Vienna, Austria, 2017, pp. 1–6.

[53] A. A. Novikov, D. Lenis, D. Major, J. Hladůvka, M. Wimmer, and K. Bühler, "Fully convolutional architectures for multiclass segmentation in chest radiographs," *IEEE Trans. Med. Imag.*, vol. 37, no. 8, pp. 1865–1876, Aug. 2018.

[54] I. Fotina, C. Lütgendorf-Caucig, M. Stock, R. Pötter, and D. Georg, "Critical discussion of evaluation parameters for inter-observer variability in target definition for radiation therapy," *Strahlentherapie und Onkologie*, vol. 188, pp. 160–167, Jan. 2012.

[55] F. Andrade and E. V. Carrera, "Supervised evaluation of seed-based interactive image segmentation algorithms," in *Proc. 20th Symp. Signal Process., Images Comput. Vis. (STSIVA)*, Bogota, Colombia, Sep. 2015, pp. 1–7.
[56] R. Rashid, M. U. Akram, and T. Hassan, "Fully convolutional neural network for lungs segmentation from chest X-rays," in *Proc. Int. Conf. Image Anal. Recognit. (ICIAR)*, Jun. 2018, pp. 71–80.
[57] S. Vajda, A. Karargyris, S. Jaeger, K. C. Santosh, S. Candemir, Z. Xue, S. Antani, and G. Thoma, "Feature selection for automatic tuberculosis screening in frontal chest radiographs," *J. Med. Syst.*, vol. 42, no. 8, pp. 146–158, Aug. 2018.
[58] K. C. Santosh and S. Antani, "Automated chest X-ray screening: Can lung region symmetry help detect pulmonary abnormalities?" *IEEE Trans. Med. Imag.*, vol. 37, no. 5, pp. 1168–1177, May 2018.

TAO PENG is currently pursuing the Ph.D. degree with Soochow University, China. His main research interests include medical image processing and analysis, pattern recognition, machine learning, and their applications. He is a member of CCF.

YIHUAI WANG received the Ph.D. degree from Hohai University, Nanjing, China. He is currently a Professor with Soochow University, Suzhou, China. He is also the Director of embedded system and Internet of things technical committee, Jiangsu Computer Federation. He is also the Director of embedded system and Internet of things Research Institute, Soochow University. His research interests include parallel systems, software engineering, embedded system and application, artificial intelligence, and pattern recognition. He is a Senior Member of CCF.

THOMAS CANHAO XU received the M.Eng. degree from Zhejiang University, China, in 2007, and the D.Sc. degree from the University of Turku, Finland, in 2012. He has been a System Engineer and Analyst for several projects, since 2005. From 2008 to 2016, he was with the Software Engineering Laboratory and Computer Systems Laboratory, University of Turku, as a Researcher, a Postdoctoral, and a Teaching Staff. He has been involved in several projects of Academy of Finland, EU, and China. He is currently an Adjunct Professor with Soochow University, China. He has authored and coauthored over 50 international refereed articles. His research interests include pattern recognition, machine learning, and their applications. He has been a member of ACM, since 2007.

XINJIAN CHEN received the Ph.D. degree from the Center for Biometrics and Security Research, Key Laboratory of Complex Systems and Intelligence Science, Institute of Automation, Chinese Academy of Sciences, Beijing, China, in 2006. After completing the graduation, he joined Microsoft Research Asia, where he was involved in research on handwriting recognition. From 2008 to 2012, he conducted a Postdoctoral Research at several prestigious groups, such as the Medical Image Processing Group, University of Pennsylvania, Department of Radiology and Image Sciences, National Institutes of Health, and Department of Electrical and Computer Engineering, University of Iowa. In 2012, he joined the School of Electrical and Information Engineering, Soochow University, as a Full Professor. He is currently a Distinguished Professor with Soochow University, and serves as the Director of the University Level Laboratory Medical Image Processing, Analysis and Visualization Laboratory. He has authored over 70 high-quality international journal/conference articles. His research interests include medical image processing and analysis, pattern recognition, machine learning, and their applications.